

Research Papers

Ultrathin solid composite electrolytes for long-life lithium metal batteries

Lehao Liu, Jinshan Mo, Rongmin Zhou, Tianrong Yang, Rubing Xu, Jiaxin Tu, Qian Zhao, Mengxuan Zhang, Dongmei Zhang, Baoyi Wang, Dingrong Long, Kunda Yang, Jiangping Zhang, Meicheng Li*

State Key Laboratory of Alternate Electrical Power System with Renewable Energy Sources, School of New Energy, North China Electric Power University, Beijing 102206, China

ARTICLE INFO

Keywords:

Polyethylene oxide electrolyte
Aramid nanofiber
Vacuum filtration
Mechanical strength
Lithium metal battery

ABSTRACT

Polyethylene oxide (PEO)-based electrolytes are an important electrolyte for solid-state lithium metal batteries, owing to their excellent film-forming ability, superior contact with the electrodes, and cost-effectiveness. However, their application is limited by the insufficient mechanical strength and ambient-temperature ionic conductivity, and the lithium dendrite-induced problems. Especially, the conventional solution-casted polymer electrolytes possess larger thickness of $>100\ \mu\text{m}$ for suitable flexibility, but this would increase the electrolyte resistance and decrease the energy density of the batteries. Herein, an ideal aramid nanofiber (ANF)/PEO-LiTFSI composite electrolyte is prepared by a facile and environmentally-friendly vacuum filtration method. In contrast with the solution casting method followed by a slow drying process, the ANFs in the solution form 3D continuous frameworks without aggregation in the fast vacuum filtration process, resulting in a great enhancement in the mechanical strength (13 times that of the solution-casted PEO-LiTFSI electrolyte) for the ultrathin composite electrolyte of up to $16\ \mu\text{m}$. The filtered solvent in the suction flask is also recyclable without the environment pollution. Density functional theory calculations and nuclear magnetic resonance measurements confirm that a fast-ion pathway at the PEO/ANF interfaces is beneficial to increasing the ionic conductivity. Due to the improvement in the mechanical and electrical properties, the composite electrolyte-based $\text{Li}|\text{Li}$ batteries work stably for 2200 h without short-circuit. Moreover, the composite electrolyte-containing $\text{Li}|\text{LiFePO}_4$ batteries display better cycle stability than the PEO-LiTFSI electrolyte-containing batteries (95 % vs. 2 % capacity retention after 150 cycles). The composite electrolyte-based batteries can also stably cycle for 338 cycles with a high capacity retention of 90 %. This work provides a facile and eco-friendly method to prepare ultrathin and robust solid electrolytes for long-life lithium metal batteries.

1. Introduction

Lithium-ion batteries possess obvious advantages regarding energy density and cycling life [1,2], which make them applied in the fields of electronics and transportation [3]. However, the utilization of nonaqueous liquid electrolytes containing nonaqueous organic solvents causes a series of problems such as electrolyte leakage, corrosion of electrode materials, dendrite growth, and explosion at high temperatures [4–6]. Replacing liquid electrolytes with solid-state electrolytes is considered as an important route to improve the safety and energy density of lithium-ion batteries [7,8].

Solid polymer electrolytes have unique merits such as excellent film formation ability, good contact with the electrodes, light weight, easy

preparation and low cost, showing great potential in high-energy-density lithium metal batteries [9,10]. However, the accompanied disadvantages, such as low mechanical strength and room-temperature ionic conductivity, hinder the application of the electrolytes [11].

A few methods including polymer molecular structure design, addition of plasticizers, blending with other polymers and nanoparticle filling are developed to tackle these problems [12–14]. Among them, the addition of nanoparticles such as TiO_2 [15,16], BN [17,18] and SiO_2 [19–22] into the polymer matrices would not only increase the mechanical strength of the electrolytes, but also elevating the conductivity by prohibiting the polymer crystallization and forming a fast-ion pathway at the polymer/nanofiller interfaces [23–27]. Nevertheless, the agglomeration of the high-surface-area nanofillers and the failure to

* Corresponding author.

E-mail address: mcli@ncepu.edu.cn (M. Li).

<https://doi.org/10.1016/j.est.2025.115777>

Received 16 December 2024; Received in revised form 25 January 2025; Accepted 5 February 2025

Available online 11 February 2025

2352-152X/© 2025 Elsevier Ltd. All rights are reserved, including those for text and data mining, AI training, and similar technologies.

generate long-distance nanofiller networks remain as a challenge, greatly weakening the properties of the composite polymer electrolytes (CPEs) [28,29]. Moreover, the CPEs, which are prepared by the conventional solution casting or coating method with a subsequent heating drying process, usually have large thickness of $>100\ \mu\text{m}$ for suitable mechanical flexibility, but this would increase the electrolyte resistance and decrease the energy density of the batteries, hindering the application of the CPEs in solid-state lithium metal batteries. Although a few methods such as solution filling and coating have been used for preparing thin electrolytes, the processes are complicated and costly and the evaporation of the solutions causes environmental pollution [30–33]. Thus, it is urgent to develop an environmentally-friendly method to prepare thin CPEs with continuous nanofiller networks for high mechanical and electrical properties.

In this work, an ultrathin and robust aramid nanofiber (ANF)/polyethylene oxide (PEO)-LiTFSI CPE membrane is prepared by a novel yet facile vacuum filtration method followed by a drying process (Fig. 1a). Because of the hydrogen bonding interaction among the amide groups, the long ANFs easily form 3D continuous networks without aggregation during the short-time vacuum drying process, resulting in the great enhancement in the mechanical strength for the ultrathin CPE (Fig. 1b-c). By adjusting the ANF content, the thickness of the CPE membrane can be decreased to $16\ \mu\text{m}$, which is comparable to that of the commercial separators. The PEO/ANF interfaces work as a fast-ion pathway to increase the ionic conductivity by prohibiting the PEO crystallization and promoting the LiTFSI dissociation through the hydrogen bonding between the PEO/TFSI⁻ and the ANFs. Moreover, the solvent in the suction flask is recyclable, which not only avoids the environmental pollution but also reduces the preparation cost. Owing to the great improvement in the mechanical and electrical properties, the ultrathin CPE-based Li||

Li cells achieve stable plating/stripping for 2200 h, and the solid-state lithium metal batteries show outstanding cycling stability, indicating their great application potential.

2. Experimental section

2.1. Preparation of the electrolytes

4.00 g potassium hydroxide (KOH, Aladdin, $\geq 99.99\%$) and 4.00 g Kevlar 69 microfiber (DuPont, $\geq 99.99\%$) were added in 200.00 g dimethyl sulfoxide (DMSO, Alfa, $\geq 99.99\%$) and then stirred for 14 days to obtain a dark red ANF solution. A certain amount of the ANF solution containing 15.00 mg ANF was mixed with 30.00 mL DMSO under strong stirring to obtain a diluted ANF/DMSO solution. The PEO/H₂O solutions were obtained by dissolving 5.00, 10.00, 15.00 and 45.00 mg PEO (Macklin, Mw: 600,000) in 8.00 mL deionized water under stirring, respectively. The ANF/DMSO solution and the PEO/H₂O solution were then mixed and agitated for 24 h to prepare a homogeneous ANF/PEO solution.

The ANF/PEO-LiTFSI electrolyte membranes were prepared by a vacuum filtration method followed by a vacuum drying process. Firstly, the ANF/PEO solution was filtered in vacuum with a filtration membrane (pore size: $\sim 50\ \text{nm}$) to obtain the ANF/PEO gel membranes. Subsequently, 2 or 5 mL 1 M LiTFSI/ethanol solution was vacuum filtered to fabricate ANF/PEO-LiTFSI gel membranes. After that, ultrathin ANF/PEO-LiTFSI electrolyte membranes were obtained by peeling the ANF/PEO-LiTFSI gel membranes off from the filter membranes and desiccated in vacuum at $40\ ^\circ\text{C}$. The collected solution in the filter bottle underwent purification through evaporation at $60\ ^\circ\text{C}$ in vacuum to remove water and then centrifugation to remove the PEO residual, and

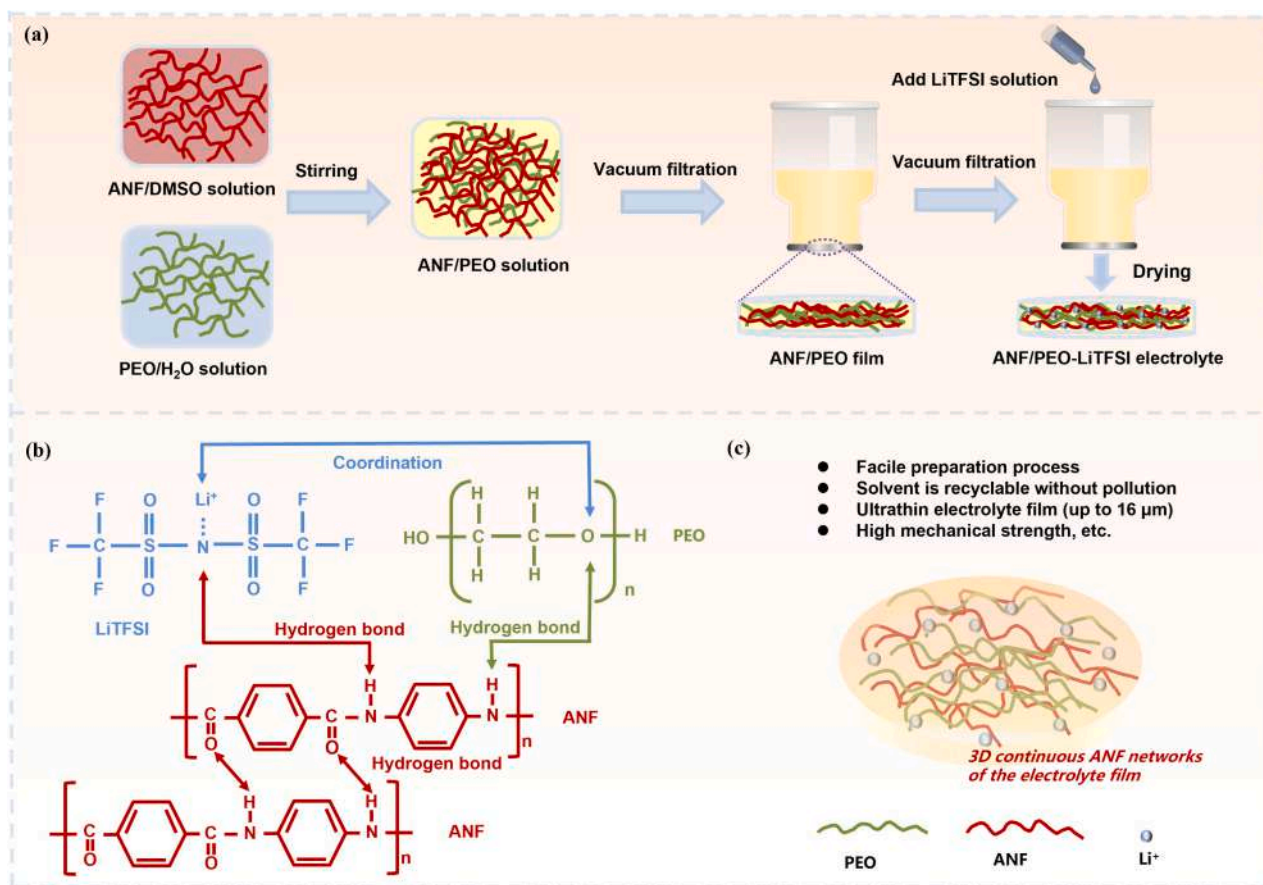


Fig. 1. Preparation process of ultrathin electrolytes. (a) Schematic illustration of the fabrication procedure of ultrathin composite electrolytes of ANF/PEO-LiTFSI by a vacuum filtration method. (b) Interactions among PEO, LiTFSI and ANF. (c) Advantages of the electrolyte preparation method.

the pure and expensive DMSO solvent was then reused in subsequent experiments. The CPE membranes using 2 mL LiTFSI solution and 45.00, 15.00, 10.00 and 5.00 mg PEO were denoted as 2ANF5Li, 2ANF10Li, 2ANF25Li and 2ANF40Li, respectively (i.e., the ANF weight ratios of the CPEs were around 5 %, 10 %, 25 % and 40 %, respectively). Similarly, the CPE membranes using 5 mL LiTFSI solution and 10.00 and 5.00 mg PEO were denoted as 5ANF25Li and 5ANF40Li, respectively. The 2ANF0Li, 5ANF5Li and 5ANF10Li CPEs were not obtained because of their low mechanical strength and the difficulty in peeling them off from the filter membranes.

For comparison, the conventional solution-casted PEO-LiTFSI electrolyte was obtained by dispersing 1.83 g PEO and 0.66 g LiTFSI in 50 mL acetonitrile (Aladdin, $\geq 99.90\%$) at 40 °C for 24 h under strong stirring, putting them in a Teflon mold, and then exsiccating them at 60 °C for 48 h in vacuum condition. All the electrolytes were cut into small discs and then kept in an argon-containing glove box before use.

2.2. Characterizations

The morphology of the electrolytes was detected using a SU8010 scanning electron microscope (SEM). A D8 Focus X-ray diffractometer (XRD) was utilized to investigate the crystallinity of the electrolytes. The thermal stability of the electrolytes was detected by a thermogravimetric analyzer (TGA) in nitrogen at 10 °C min⁻¹. The mechanical property of the electrolyte films was tested using a JB-126A tensile tester at 2 mm min⁻¹. A Fourier transform infrared spectrometer (FT-IR) was utilized to determine the change of the chemical bonding and functional groups of PEO, LiTFSI and ANF using an ATR mode at 400–4000 cm⁻¹. A solid-state nuclear magnetic resonance spectrometer (ssNMR) was employed to perform ⁷Li magic angle spinning at 12 kHz. The spectra were obtained using LiCl as a reference. Differential scanning calorimetry (DSC) tests were taken to detect the crystallinity of the electrolytes in a temperature range from -90 to 110 °C in nitrogen. The PEO crystallinity (χ) of the electrolytes was calculated according to Eq. (1):

$$\chi = (\Delta H / F \cdot \Delta H_0) \cdot 100\% \quad (1)$$

where ΔH is the enthalpy change of the CPEs, ΔH_0 is the melting enthalpy of PEO (i.e., 213.7 J g⁻¹), and F is the mass ratio of PEO in the electrolytes.

Density functional theory (DFT) was utilized to obtain the migration energy barrier of Li⁺ along the PEO chain and the ANF/PEO interface. The DFT calculations were performed within the DFT framework on Vienna ab initio Simulation Package with the Perdew-Burke-Ernzerhof (PBE) form of generalized-gradient approximation (GGA) exchange-correlation energy function using VMD and Gaussian16 software for the visualization.

2.3. Electrochemical measurements

The electrolyte-based CR2032 coin-type batteries were assembled for various electrochemical characterizations. An electrochemical workstation (Zahner Zennium) was employed to detect the impedance change of the stainless steel (SS)|electrolyte|SS cells at 30–80 °C. The ionic conductivity (σ) of the electrolytes was calculated according to Eq. (2):

$$\sigma = L / (R \cdot S) \quad (2)$$

where L is the electrolyte thickness, R is the resistance, and S is the contact area. Linear sweep voltammetry (LSV) measurements of the Li|electrolyte|SS cells were performed using a CHI660E electrochemical workstation at 1 mV s⁻¹ in a potential range from 2 to 6 V at 60 °C. The critical current density (CCD) and cycling duration (0.1 mA cm⁻², 0.1 mAh cm⁻²) of the Li|electrolyte|Li batteries were detected using a Neware battery test system. The solid-state Li|electrolyte|LiFePO₄ batteries were prepared with Li foil anodes and ~2 mg cm⁻² LiFePO₄

containing cathodes, and their electrochemical performance was then detected between 2.5 and 3.8 V at 60 °C using different C rates (1 C = 170 mAh g⁻¹). The Li|electrolyte|LiNi_{0.6}Co_{0.2}Mn_{0.2}O₂ batteries were prepared with Li foil anodes and ~2 mg cm⁻² LiNi_{0.6}Co_{0.2}Mn_{0.2}O₂-containing cathodes, and their electrochemical performance was then detected between 2.8 and 4.2 V at 30 °C using different C rates (1 C = 180 mAh g⁻¹). 20 μ L 1 M LiPF₆ in EC:DMC:DEC (1:1:1 in vol%) with 1 % FEC (Dodo Chem) was added on the cathodes to improve the cathode/electrolyte interfacial contact and protect the cathodes.

3. Results and discussion

3.1. Morphology of the electrolytes

The ANF/PEO-LiTFSI CPEs containing different content of ANF were prepared by the facile vacuum filtration method, and their optical photographs are shown in Fig. S1. The CPEs have good film-forming ability, and their color becomes darker gradually with the increase of the ANF content. The uniform color distribution indicates that the ANFs are uniformly dispersed in the CPEs, which was attributed to the short-time vacuum filtration process avoiding the ANF agglomeration effectively. Moreover, all the CPE membranes even with high ANF contents (i.e., 2ANF5Li, 2ANF10Li, 2ANF25Li, 2ANF40Li, 5ANF25Li and 5ANF40Li) are semi-transparent, implying the small thickness of the electrolytes.

The morphology characteristics of the composite electrolytes were revealed by SEM (Figs. 2 and S2). The 2ANF5Li electrolyte with a low ANF content has a smooth surface (Fig. 2a), while the surface becomes rougher with higher ANF content (Fig. 2b-c), because of the interconnection of the ANFs. The 2ANF5Li and 2ANF10Li electrolytes show small thicknesses of 16 and 23 μ m, respectively (Fig. 2e-f). When increasing the ANF and LiTFSI contents, the thickness of the 5ANF25Li electrolyte increased to 39 μ m (Fig. 2g), which is comparable to that of the commercial polymer separators. The PEO-LiTFSI electrolyte film was also fabricated by the conventional solution casting method, and it has a similar surficial characteristic to the solution-filtrated electrolytes (Fig. 2d). However, the solution-casted PEO-LiTFSI electrolyte shows a thickness of 187 μ m (Fig. 2h), which is much larger than those of the vacuum filtrated CPEs. In short, ultrathin ANF/PEO-LiTFSI CPE membranes are successfully prepared by the novel vacuum filtration method.

3.2. Electrochemical and mechanical properties

Electrochemical stability is one of the important standards of the electrolytes, and it is related to the application in lithium batteries. The LSV measurements were taken to examine the electrochemical stability of the electrolytes (Fig. 3a). The PEO-LiTFSI electrolyte shows a narrow electrochemical oxidization window of 3.8 V. In comparison, the electrochemical oxidization windows of the 2ANF5Li and 2ANF10Li electrolytes increase to 4.8 V, indicating the positive effect of the ANFs. The 5ANF25Li electrolyte with a high LiTFSI content also displays a wide oxidization window of 4.5 V, suggesting its compatibility with high-voltage electrodes. The enhanced electrochemical oxidation stability of the PEO-based electrolyte by the ANF incorporation should be ascribed to the inhibition of the decomposition of PEO and TFSI⁻ by the hydrogen bonding interactions between the amide groups in the ANFs and the —O— groups in the PEO chains and the TFSI⁻ anions from the lithium salt.

The tensile properties of the electrolytes were also tested, and the stress-strain curves of the electrolytes are presented in Fig. 3b. The ultimate mechanical strength and Young's modulus of the PEO-LiTFSI electrolyte are 0.20 and 0.07 MPa, respectively, and the large ultimate tensile strain of 127.52 % is due to the high flexibility of PEO. In contrast, the 2ANF5Li electrolyte shows high mechanical strength and Young's modulus of 0.34 and 0.17 MPa, respectively, due to the incorporation of the 3D ANF frameworks. The 2ANF10Li electrolyte also

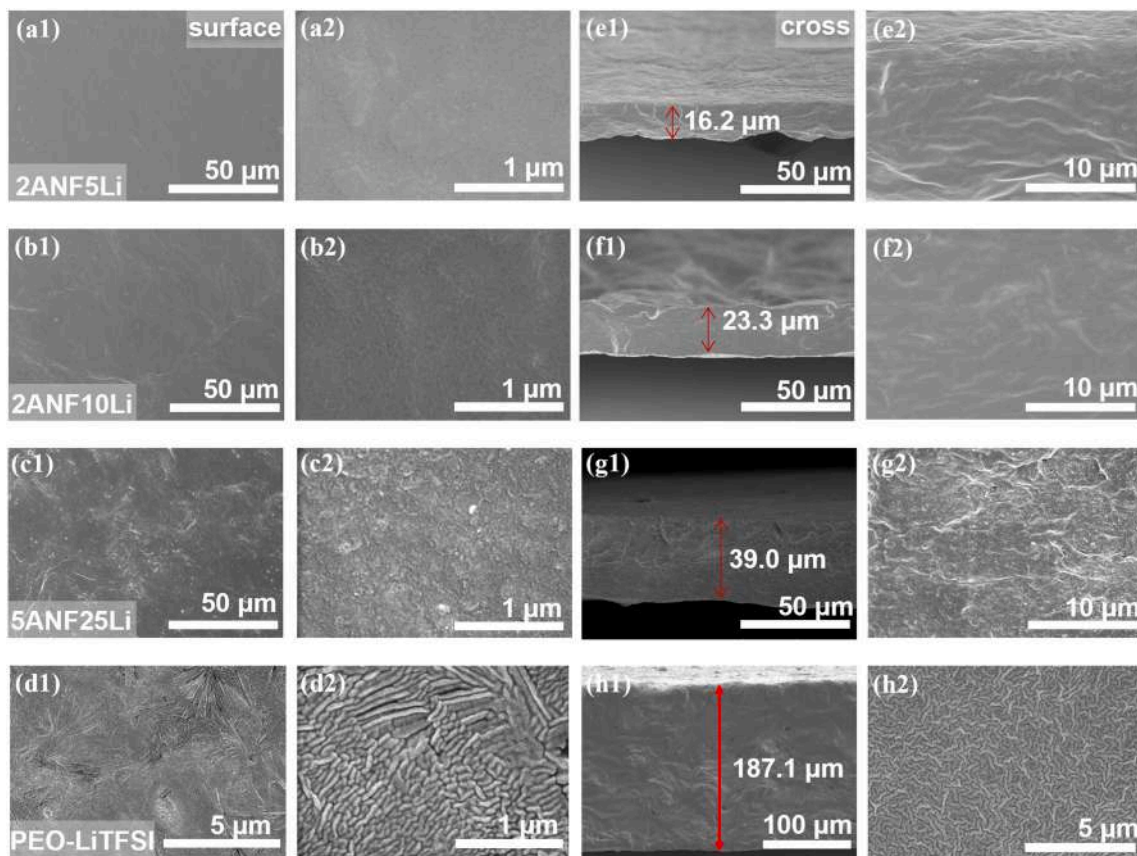


Fig. 2. Morphology of the electrolytes. (a1-a2, b1-b2, c1-c2 and d1-d2) Surficial and (e1-e2, f1-f2, g1-g2, and h1-h2) cross-sectional SEM images of (a1-a2 and e1-e2) 2ANF5Li, (b1-b2 and f1-f2) 2ANF10Li, (c1-c2 and g1-g2) 5ANF25Li, and (d1-d2 and h1-h2) PEO-LiTFSI electrolytes.

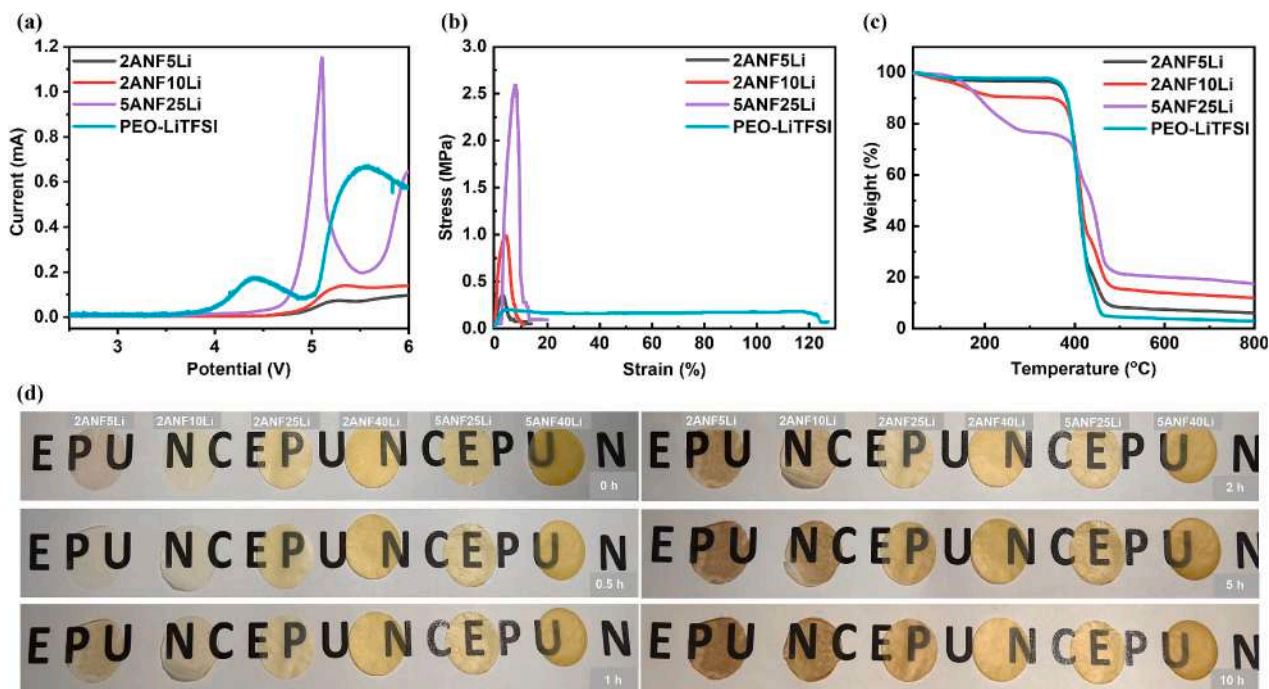


Fig. 3. Electrochemical and mechanical properties. (a) LSV curves of the electrolytes. (b) Tensile stress-strain curves of the electrolytes. (c) TGA curves of the electrolytes. (d) Optical photos of the electrolyte discs at 160 °C for 0, 0.5, 1, 2, 5 and 10 h (from left to right: 2ANF5Li, 2ANF10Li, 2ANF25Li, 2ANF40Li, 5ANF25Li and 5ANF40Li electrolytes).

shows high mechanical strength and Young's modulus of 0.98 and 0.46 MPa, respectively. When increasing the ANF content, the mechanical strength and Young's modulus of the 5ANF25Li electrolyte reach 2.59 and 1.21 MPa, which are 13 and 17 times those of the PEO-LiTFSI electrolyte, respectively. This also explains why the ultrathin ANF/PEO-LiTFSI CPE membranes can be easily prepared. The high Young's modulus of the CPEs is beneficial for the inhibition of the lithium dendrites [34].

The thermostability of the electrolytes was detected by the TGA measurements (Fig. 3c). All the electrolytes have <2.7 wt% loss below 100 °C, suggesting the low-content solvent in the electrolytes. The mass loss at 140–300 °C and ~400 °C are related to the decomposition of LiTFSI and PEO, respectively. The various weight loss behavior at 140–300 °C may be ascribed to the differences in the LiTFSI content and the ANF microstructure of the electrolytes (especially, the higher LiTFSI content in the 5ANF25Li electrolyte). The residual amounts of the 2ANF5Li, 2ANF10Li and 5ANF25Li CPEs are 6.0 %, 11.9 % and 17.3 % at 800 °C, respectively, which are consistent with the ANF contents of the CPEs. This also implies the high thermostability of the ANF-based CPEs.

To further assess the thermostability of the CPEs, the electrolyte discs were kept at 160 °C for different time, and the change in the shape and the molten state of the electrolytes was also observed (Fig. 3d). It can be found that only a small portion of the 2ANF5Li electrolyte shrank after 10 h, and the others still maintained their original shapes without being molten, again proving the greatly-improved mechanical stability of the ANF-based CPEs.

3.3. Electrical properties and ion conduction mechanism

Fig. 4a presents the Arrhenius plots of the ionic conductivities of the CPEs at 30–80 °C. The 2ANF5Li electrolyte shows a low ionic conductivity of $2.94 \times 10^{-6} \text{ S cm}^{-1}$ at 30 °C, but its ionic conductivity increases to $1.29 \times 10^{-4} \text{ S cm}^{-1}$ at 60 °C, because of the decrease of the

crystallization of PEO. When increasing the ANF content, the 2ANF10Li electrolyte exhibits a much higher ionic conductivity of $1.73 \times 10^{-5} \text{ S cm}^{-1}$ at 30 °C. However, the 2ANF25Li and 2ANF40Li electrolytes with more inert ANFs have much lower ionic conductivities of 9.66×10^{-7} and $7.82 \times 10^{-7} \text{ S cm}^{-1}$ at 30 °C, respectively. When increasing the LiTFSI content, the 5ANF25Li electrolyte also displays a high ionic conductivity of $1.55 \times 10^{-5} \text{ S cm}^{-1}$ at 30 °C.

High-crystallinity PEO with slow movement ability has an adverse effect on the ionic conductivity of the electrolytes. To reveal the effect of the ANF addition on the PEO crystallinity, XRD characterizations have been performed (Fig. 4b). The solution-casted PEO-LiTFSI electrolyte has two distinct characteristic peaks at around 19° and 23°, which are related to the PEO crystallization. However, these peak intensity decreases greatly in the 2ANF5Li, 2ANF10Li and 5ANF25Li electrolytes, indicating that the ANF-containing electrolytes are nearly in an amorphous state. This also means that the ANF addition can effectively decrease the crystallinity of the PEO matrices, which is helpful for facilitating the ionic transport of the CPEs at room temperature.

DSC measurements were then performed to verify the positive effect of the ANFs on inhibiting the PEO crystallization (Fig. 4c). The glass transition temperature of the PEO-LiTFSI electrolyte is -59.7 °C, while the 2ANF5Li and 2ANF10Li electrolytes have lower glass transition temperatures of -61.1 and -62.7 °C, respectively, because of the incorporation of the uniformly-dispersed ANFs in the electrolytes. Moreover, the PEO crystallinity of the PEO-LiTFSI electrolyte is 12.2 %. In contrast, the 2ANF5Li electrolyte has a much lower PEO crystallinity of 6.2 %, and the 2ANF10Li and 5ANF25Li electrolytes containing more ANFs are in an amorphous state. Combined with the DSC and XRD results, it is easily concluded that the incorporation of the ANFs can greatly decrease the PEO crystallinity of the electrolytes.

FT-IR spectroscopy was employed to disclose the impact of the ANFs on the ionic conductivity of the electrolytes (Fig. S3). The PEO-LiTFSI electrolyte shows some characteristic peaks at 788, 948, 959, 1058 and 1097 cm^{-1} , related to the tensile and bending vibration modes of

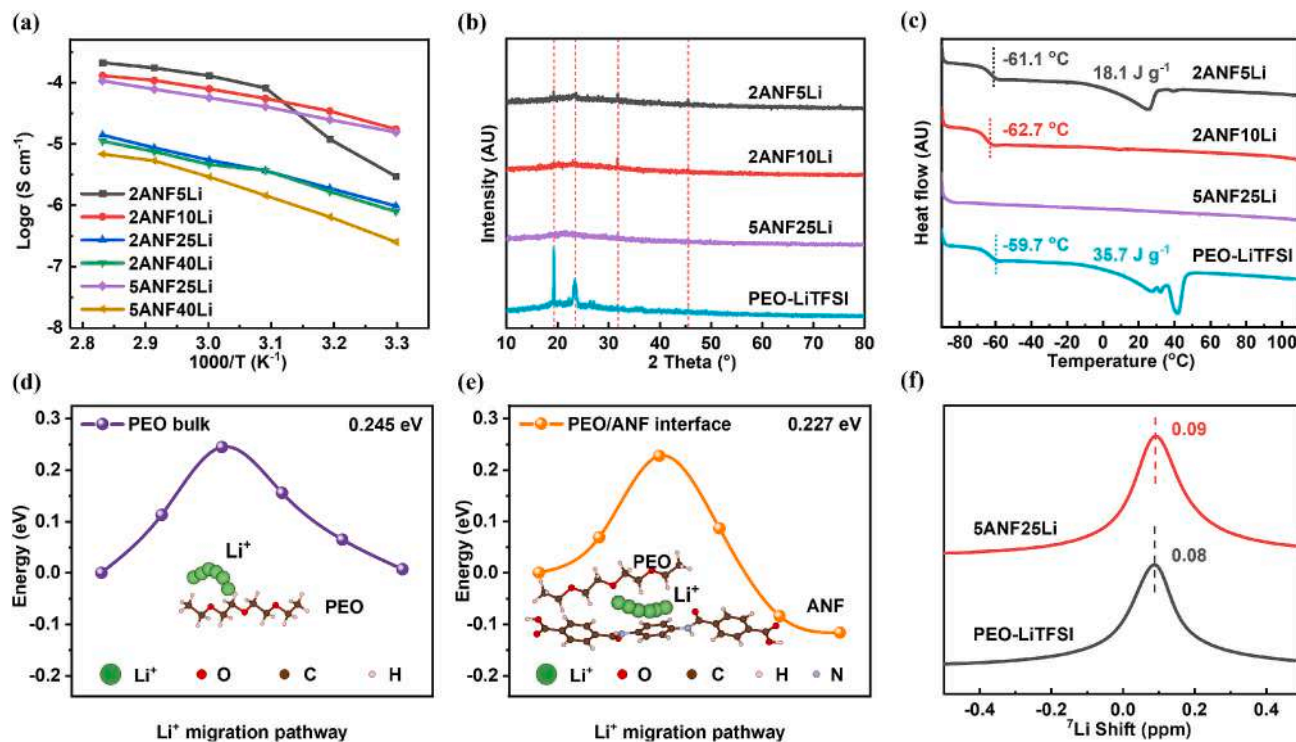


Fig. 4. Electrical properties and ion conduction mechanism of the electrolytes. (a) Ionic conductivity of the electrolytes at various temperatures. (b) XRD patterns of the electrolytes. (c) DSC curves of the electrolytes. Li^+ migration energy barriers (d) in the PEO bulk and (e) at the PEO/ANF interface. (f) ^7Li ssNMR spectra of PEO-LiTFSI and 5ANF25Li electrolytes.

the C-O-C and C=O groups of PEO. However, the peak at 948 cm^{-1} in the PEO-LiTFSI electrolyte moves to 952 cm^{-1} in the ANF-based electrolytes, and the peak at 1097 cm^{-1} in the PEO-LiTFSI film almost disappears in the ANF-containing electrolytes (or the peak intensity becomes much poorer). Meanwhile, the N-H group-related peaks at 1512 and 3320 cm^{-1} in the ANFs nearly disappear in the ANF-containing electrolytes. This should be attributed to the hydrogen bonding interaction between the N-H groups of the ANFs and the C-O-C groups of PEO [35,36], resulting in the decrease of the PEO crystallinity of the ANF-containing electrolytes. Moreover, the S-O and -CF₃ group-related peaks at 654 and 761 cm^{-1} in the PEO-LiTFSI electrolyte shift (to ~ 655 and $\sim 762\text{ cm}^{-1}$, respectively), implying the hydrogen bonding interaction between the TFSI⁻ anions and the N-H groups of the ANFs. This is conducive to the LiTFSI dissociation for providing free Li⁺ ions.

Thus, the ANFs play dual roles in increasing the ionic conductivity of the composite electrolytes by preventing the crystallization of PEO and accelerating the dissociation of LiTFSI.

In order to clarify the Li⁺ pathways in the electrolytes, the Li⁺ migration energy barrier was also obtained based on the DFT calculations (Fig. 4d-e). The Li⁺ migration barrier along the PEO chains is 0.245 eV . In comparison, the Li⁺ migration barrier at the PEO/ANF interfaces decreases to 0.227 eV , indicating that Li⁺ ions prefer to move at the PEO/ANF interfaces, which act as a fast-ion pathway in the composite electrolytes. The ssNMR spectra further disclose that the ⁷Li peak width in the PEO-LiTFSI electrolyte becomes broader when adding the ANFs (Fig. 4f), again implying the fast-ion pathway in the composite electrolytes [37].

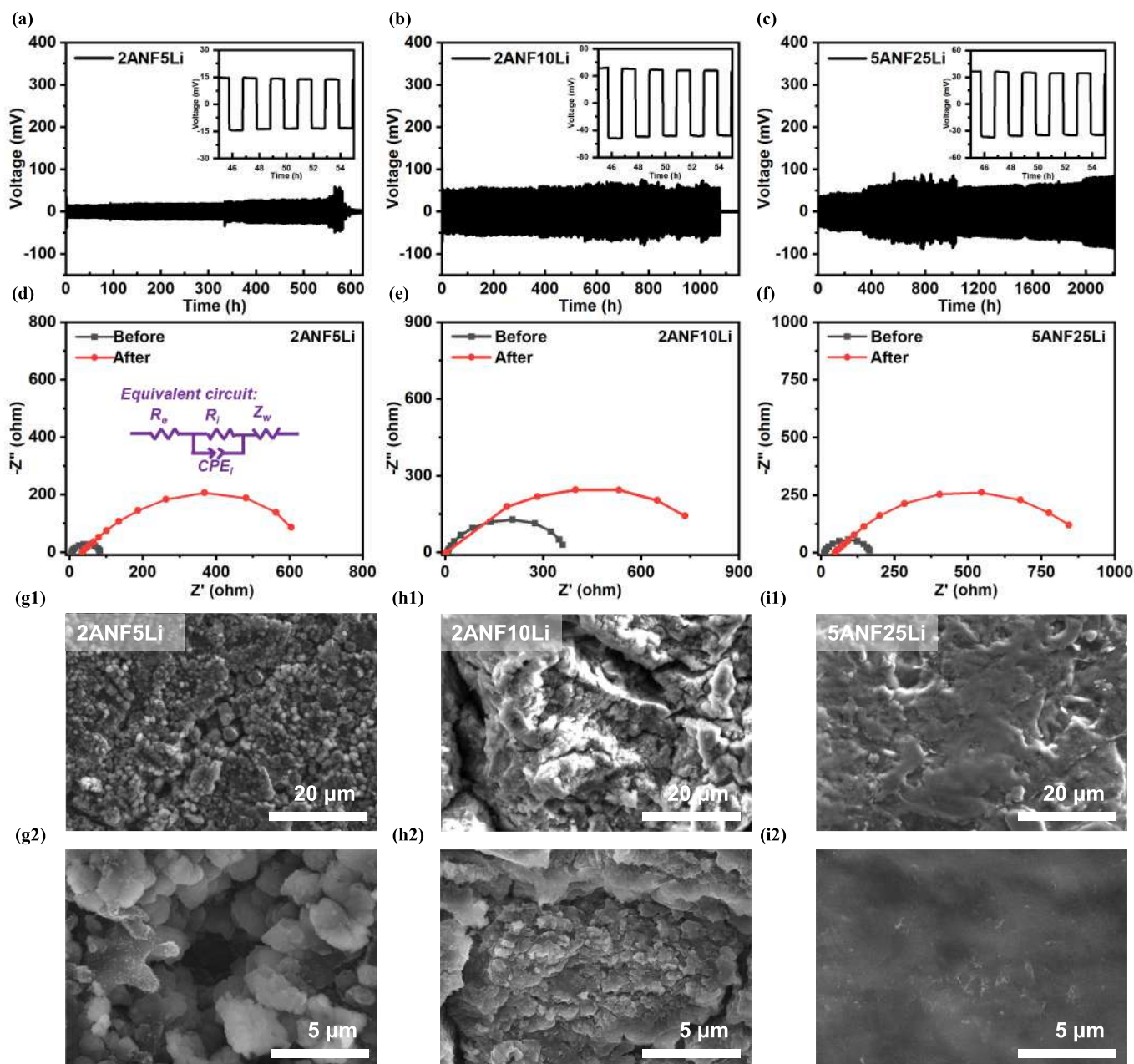


Fig. 5. Li[electrolyte]Li battery performance. Galvanostatic cycling curves of (a) 2ANF5Li, (b) 2ANF10Li and (c) 5ANF25Li electrolyte-based Li||Li symmetric batteries at 0.10 mA cm^{-2} and 60 °C . The insets are the corresponding enlarged cycling curves. Electrochemical impedance spectra of the Li||Li batteries with (d) 2ANF5Li, (e) 2ANF10Li and (f) 5ANF25Li electrolytes before and after the cycling process. An equivalent circuit model is shown in Fig. 5d. SEM images of the electrochemically cycled Li electrodes in (g) 2ANF5Li, (h) 2ANF10Li and (i) 5ANF25Li electrolyte-based Li||Li batteries.

3.4. Resistance against lithium dendrites

To evaluate the resistance of the CPEs against the growth of lithium dendrites, the CPE-based Li||Li batteries were galvanically cycled at 60 °C with increasing current densities (Fig. S4). The 2ANF10Li electrolyte-based Li||Li cell shows a much higher CCD of 1.65 mA cm⁻² than the 2ANF5Li electrolyte-based cell (0.60 mA cm⁻²), owing to the greatly-enhanced mechanical strength of the electrolyte with more ANFs. The CCD of the 5ANF25Li electrolyte-based Li||Li cell decreases to 0.30 mA cm⁻², which should be attributed to the low ionic conductivity of the electrolyte.

The cycling duration of the Li|electrolyte|Li cells was evaluated at 60 °C and 0.1 mA cm⁻² (area capacity: 0.1 mAh cm⁻²). The potential of the PEO-LiTFSI electrolyte-based Li||Li cell quickly increased to ~200 mV after 284 h, however, the potential dropped to 0 V suddenly, indicating the short-circuit of the cell (Fig. S5). In stark contrast, the 2ANF5Li, 2ANF10Li and 5ANF25Li CPE-based cells cycled stably for 584, 1075 and 2200 h without short-circuit (Fig. 5a-c), showing the greatly-enhanced ability of the CPEs to inhibit the growth of lithium dendrites. The 5ANF40Li CPE-based cell can also work for 2200 h, but the potential is higher than those of the 2ANF5Li, 2ANF10Li and 5ANF25Li CPE-based cells, because of the low ionic conductivity of the 5ANF40Li CPE. Further galvanostatic cycling under a higher current

density of 0.2 mA cm⁻² (area capacity: 0.2 mAh cm⁻²) at 60 °C also showed that the 5ANF25Li electrolyte-based cell had better cycle performance than the PEO-LiTFSI, 2ANF5Li and 2ANF10Li electrolyte-based batteries (Fig. S6a-d).

The EIS spectra of the Li|electrolyte|Li cells cycled at 0.1 mA cm⁻² (area capacity: 0.1 mAh cm⁻²) are also shown in Fig. 5d-f to investigate the resistance change of the cells. The semicircles in the high-frequency and the low-frequency regions in the Nyquist diagrams are corresponded to the ohmic resistance (R_o) of the electrolyte and the electrolyte/electrode interface resistance (R_i), respectively [23]. The 2ANF5Li electrolyte-based Li||Li cell showed an initial R_i value of 76 Ω, but the R_i value soon increased to 569 Ω in 584 h. In comparison, the R_i value of the 5ANF25Li electrolyte-based Li||Li cell increased slowly from 155 Ω to 796 Ω during the long-time cycling of 2200 h, because of the high mechanical strength of the 5ANF25Li electrolyte and the superior ability to inhibit the lithium dendrite growth. The EIS spectra of the Li||Li cells at 0.2 mA cm⁻² (area capacity: 0.2 mAh cm⁻²) further indicated that the 5ANF25Li electrolyte-based cell maintained lower resistances after the cycling (Fig. S6e-h).

The surface morphology of the Li electrodes after the cycling at 0.1 mA cm⁻² in the Li||Li symmetric cells was then detected by SEM (Fig. 5g-i). There are numerous particles and cracks on the Li electrodes in the 2ANF5Li and 2ANF10Li electrolyte-based cells after the cycling

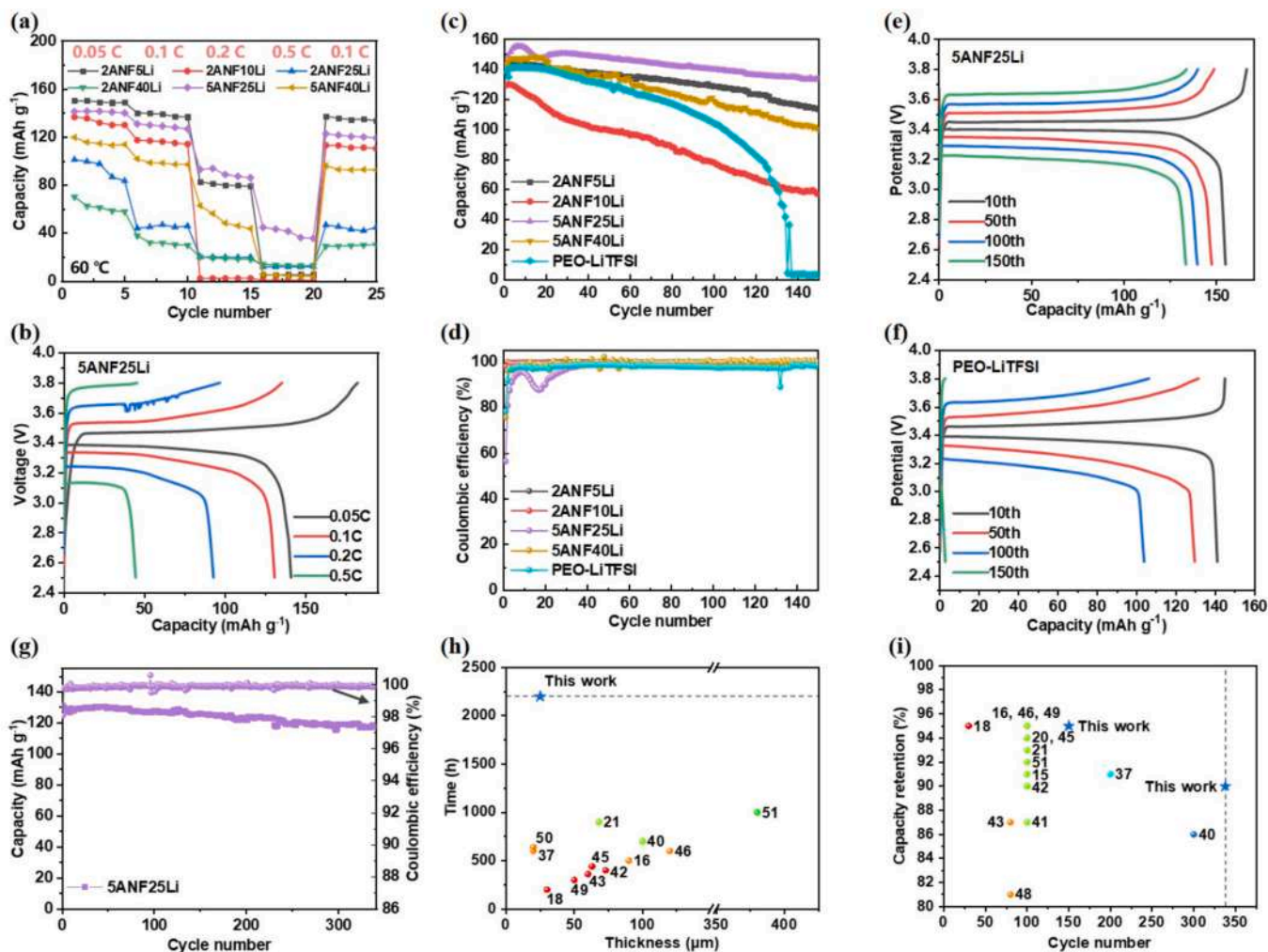


Fig. 6. Solid-state lithium metal battery performance. (a) Rate performance of Li|electrolyte|LiFePO₄ batteries at 60 °C, and (b) the corresponding charge and discharge voltage profiles of 5ANF25Li CPE-based batteries at different rates. (c) Cycling performance and (d) Coulombic efficiency of the batteries at 60 °C and 0.1 C. The corresponding charge and discharge voltage profiles of (e) 5ANF25Li and (f) PEO-LiTFSI electrolyte-based batteries. (g) Cycling performance and Coulombic efficiency of 5ANF25Li electrolyte-based Li||LiFePO₄ batteries at 0.2C and 60 °C. Comparison of (h) the electrolyte thickness and Li||Li cell cycle stability, and (i) ASLMB cycling performance recently reported in the open literatures (Table S1).

for 584 and 1075 h, respectively. In contrast, the surface of the Li electrodes in the 5ANF25Li electrolyte-based cell remained smooth and dense after the cycling for 2200 h, again indicating the more uniform Li deposition and the effective suppression of Li dendrites by the 5ANF25Li electrolyte.

3.5. Solid-state lithium metal battery performance

In order to investigate the application of the CPEs in solid-state lithium metal batteries, the Li|electrolyte|LiFePO₄ cells were charged and discharged at 60 °C under different C rates (Fig. 6a). The 2ANF5Li electrolyte-based cell displayed high capacities of 149 and 139 mAh g⁻¹ at 0.05 C and 0.1 C, respectively. When increasing the C rate to 0.5 C, the 5ANF25Li electrolyte-based cell showed a higher capacity of 42 mAh g⁻¹ than other cells, because of the great enhancement on ionic conductivity and mechanical strength of the 5ANF25Li electrolyte. Moreover, among all the CPE-based cells, the 2ANF5Li and 5ANF25Li electrolyte-based cells exhibited smaller polarization (Figs. 6b and S7). When returning the charge and discharge rates to 0.1 C again after 20 cycles, the 2ANF5Li and 5ANF25Li electrolyte-based cells maintained 135 and 120 mAh g⁻¹, respectively, which were much higher than those of other cells (Fig. 6a).

The 2ANF5Li, 2ANF10Li, 5ANF25Li, 5ANF40Li and PEO-LiTFSI electrolyte-based Li||LiFePO₄ cells were chosen to determine the long-time cycling stability at 0.1 C and 60 °C (Fig. 6c-d). The PEO-LiTFSI electrolyte-based cell displayed an initial discharge capacity of 139 mAh g⁻¹, however, the capacity quickly dropped to 3 mAh g⁻¹ after 137 cycles with a low capacity retention of 2 %. In comparison, the 2ANF5Li CPE-based cell displayed high capacities of 138 and 113 mAh g⁻¹ at the first and 150th cycles with a high capacity retention of 82 %, respectively. Especially, the 5ANF25Li CPE-based cell exhibited much higher capacity of 134 mAh g⁻¹ and capacity retention of 95 % after 150 cycles, because of the greatly-enhanced lithium dendrite resistance (Fig. 5c). The capacity of the 5ANF25Li CPE-based cell increased at the first ten cycles, which is usually attributed to the electrode activation and the enhancement on the physical contact at the electrolyte/electrode interfaces [38]. The solid-state Li||LiFePO₄ cells also showed high Coulombic efficiencies (~100 % except the beginning cycles) during the long-time electrochemical cycling process (Fig. 6d), verifying the special advantage of the solid-state batteries compared to the liquid electrolyte-containing batteries. Besides, the 5ANF25Li electrolyte-based cell displayed lower polarization than the PEO-LiTFSI electrolyte-based cell (Fig. 6e-f), because of the lower resistance of the cell (further discussion in Fig. S8).

The impedance variation of the Li|electrolyte|LiFePO₄ cells during the electrochemical cycling process is presented in Fig. S8. The semi-circle in the high-frequency region and the intersection at the real axis are linked with the charge transfer resistance (R_{ct}) and the ohmic resistance (R_e), respectively [39]. All the solid-state lithium metal batteries exhibited low R_e and R_{ct} values before the cycling. However, the R_e and R_{ct} values of the PEO-LiTFSI electrolyte-based cell greatly increased to 106 and 20,000 Ω after the long-time electrochemical cycling. On the contrary, the ANF-containing cells displayed lower R_e and R_{ct} values after the cycling. Especially, the 5ANF25Li electrolyte-based cell showed the lowest R_e and R_{ct} values of 20 and 3028 Ω after the cycling process, respectively, further verifying the fast charge transfer in the CPE and the beneficial role of the ANF networks.

When cycled at 60 °C and 0.2 C, the 5ANF25Li CPE-based Li||LiFePO₄ cell still showed high capacities of 131 and 118 mAh g⁻¹ at the first and 338th cycles with a high capacity retention of 90 %, respectively (Fig. 6g). These data furtherly confirm the high cycling stability of the ANF-based lithium metal batteries. Compared to the previous reports [15,16,18,20,37,40–51], the ultrathin ANF-containing CPE-based Li||Li and Li||LiFePO₄ cells still exhibit superior cycling stability (Fig. 6h-i), indicating the promising application in long-life lithium metal batteries. Moreover, the Li|electrolyte|LiNi_{0.6}Co_{0.2}Mn_{0.2}O₂ cells

were cycled at 0.1 C, and the 2ANF5Li and 5ANF25Li CPE-based cells exhibited higher capacity and better cycling stability than the PEO-LiTFSI electrolyte-based cell (Fig. S9), furtherly verifying the compatibility of the CPEs with high-voltage cathodes and the beneficial effect of the ANF networks.

4. Conclusions

In summary, an ultrathin ANF/PEO-LiTFSI CPE membrane up to 16 μm in thickness was prepared by a facile and eco-friendly vacuum filtration method, which differs from the conventional solution casting/coating method followed by a long-time drying process. During the short-time vacuum filtration process, the 3D continuous ANF networks formed in the CPE with the assistance of the hydrogen bonding interaction, greatly increasing the mechanical strength (13 times that of the solution-casted PEO-LiTFSI electrolyte). The ionic conductivity of the electrolyte also increased, due to the 3D continuous fast-ion pathways at the PEO/ANF interfaces. As a consequence, the ultrathin CPE-based lithium symmetric batteries cycled stably for 2200 h without short-circuit. Furthermore, the Li|CPE|LiFePO₄ batteries displayed superior cycling stability than the PEO-LiTFSI electrolyte-based batteries (95 % vs. 2 % after 150 cycles). The ANF-containing batteries also demonstrated long-term cycling stability during 338 cycles. Thus, this work presents an effective way to achieve ultrathin and robust solid electrolytes for long-life lithium metal batteries.

CRedit authorship contribution statement

Lehao Liu: Writing – review & editing, Writing – original draft, Visualization, Validation, Supervision, Software, Resources, Project administration, Methodology, Investigation, Funding acquisition, Formal analysis, Data curation, Conceptualization. **Jinshan Mo:** Visualization, Validation, Supervision, Software, Methodology, Investigation, Formal analysis, Data curation. **Rongmin Zhou:** Visualization, Validation, Supervision, Software, Methodology, Investigation, Formal analysis, Data curation. **Tianrong Yang:** Software, Formal analysis, Data curation. **Rubing Xu:** Software, Formal analysis, Data curation. **Jiaxin Tu:** Software, Formal analysis, Data curation. **Qian Zhao:** Software, Formal analysis, Data curation. **Mengxuan Zhang:** Software, Formal analysis, Data curation. **Dongmei Zhang:** Software, Formal analysis, Data curation. **Baoyi Wang:** Software, Formal analysis, Data curation. **Dingrong Long:** Software, Formal analysis, Data curation. **Kunda Yang:** Software, Formal analysis, Data curation. **Jiangping Zhang:** Software, Formal analysis, Data curation. **Meicheng Li:** Writing – review & editing, Writing – original draft, Visualization, Validation, Supervision, Software, Resources, Project administration, Methodology, Investigation, Funding acquisition, Formal analysis, Data curation, Conceptualization.

Declaration of competing interest

The authors declare that they have no known competing financial interests or personal relationships that could have appeared to influence the work reported in this paper.

Acknowledgments

This work is supported partially by National Natural Science Foundation of China (52272200, 52102245, 52072121), and Hebei Natural Science Foundation (E2022502022).

Appendix A. Supplementary data

Supplementary data to this article can be found online at <https://doi.org/10.1016/j.est.2025.115777>.

Data availability

Data will be made available on request.

References

- Z. Cheng, T. Liu, B. Zhao, F. Shen, H. Jin, X. Han, Recent advances in organic-inorganic composite solid electrolytes for all-solid-state lithium batteries, *Energy Storage Mater.* 34 (2021) 388–416, <https://doi.org/10.1016/j.ensm.2020.09.016>.
- R. Ren, D. Zhiqiang, L. Jingang, Y. Weisheng, S. Zizhou, Research on high-rate and repeat frequency discharge lithium battery for electromagnetic launch primary power supply, *J. Phys. Conf. Ser.* 1507 (2020) 072022, <https://doi.org/10.1088/1742-6596/1507/7/072022>.
- X.-B. Cheng, R. Zhang, C.-Z. Zhao, F. Wei, J.-G. Zhang, Q. Zhang, A review of solid electrolyte interphases on lithium metal anode, *Adv. Sci.* 3 (2016) 1500213, <https://doi.org/10.1002/adv.201500213>.
- A. Manthiram, X. Yu, S. Wang, Lithium battery chemistries enabled by solid-state electrolytes, *Nat. Rev. Mater.* 2 (2017) 16103, <https://doi.org/10.1038/natrevmats.2016.103>.
- C. Sun, J. Liu, Y. Gong, D.P. Wilkinson, J. Zhang, Recent advances in all-solid-state rechargeable lithium batteries, *Nano Energy* 33 (2017) 363–386, <https://doi.org/10.1016/j.nanoen.2017.01.028>.
- Z. Li, J. Fu, X. Zhou, S. Gui, L. Wei, H. Yang, H. Li, X. Guo, Ionic conduction in polymer-based solid electrolytes, *Adv. Sci.* 10 (2023) 2201718, <https://doi.org/10.1002/adv.202201718>.
- L. Liu, M. Li, L. Chu, B. Jiang, R. Lin, X. Zhu, G. Cao, Layered ternary metal oxides: performance degradation mechanisms as cathodes, and design strategies for high-performance batteries, *Prog. Mater. Sci.* 111 (2020) 100655, <https://doi.org/10.1016/j.pmatsci.2020.100655>.
- X. Judez, G.G. Eshetu, C. Li, L.M. Rodriguez-Martinez, H. Zhang, M. Armand, Opportunities for rechargeable solid-state batteries based on Li-intercalation cathodes, *Joule* 2 (2018) 2208–2224, <https://doi.org/10.1016/j.joule.2018.09.008>.
- Y. Zheng, Y. Yao, J. Ou, M. Li, D. Luo, H. Dou, Z. Li, K. Amine, A. Yu, Z. Chen, A review of composite solid-state electrolytes for lithium batteries: fundamentals, key materials and advanced structures, *Chem. Soc. Rev.* 49 (2020) 8790–8839, <https://doi.org/10.1039/D0CS00305K>.
- L. Yue, J. Ma, J. Zhang, J. Zhao, S. Dong, Z. Liu, G. Cui, L. Chen, All solid-state polymer electrolytes for high-performance lithium ion batteries, *Energy Storage Mater.* 5 (2016) 139–164, <https://doi.org/10.1016/j.ensm.2016.07.003>.
- S. Li, S.-Q. Zhang, L. Shen, Q. Liu, J.-B. Ma, W. Lv, Y.-B. He, Q.-H. Yang, Progress and perspective of ceramic/polymer composite solid electrolytes for lithium batteries, *Adv. Sci.* 7 (2020) 1903088, <https://doi.org/10.1002/adv.201903088>.
- F. Fu, Y. Zheng, N. Jiang, Y. Liu, C. Sun, A. Zhang, H. Teng, L. Sun, H. Xie, A dual-salt PEO-based polymer electrolyte with cross-linked polymer network for high-voltage lithium metal batteries, *Chem. Eng. J.* 450 (2022) 137776, <https://doi.org/10.1016/j.cej.2022.137776>.
- S. Klongkan, J. Pumchusak, Effects of nano alumina and plasticizers on morphology, ionic conductivity, thermal and mechanical properties of PEO-LiCF₃SO₃ solid polymer electrolyte, *Electrochim. Acta* 161 (2015) 171–176, <https://doi.org/10.1016/j.electacta.2015.02.074>.
- L. Liu, J. Mo, J. Li, J. Liu, H. Yan, J. Lyu, B. Jiang, L. Chu, M. Li, Comprehensively-modified polymer electrolyte membranes with multifunctional PMIA for highly-stable all-solid-state lithium-ion batteries, *J. Energy Chem.* 48 (2020) 334–343, <https://doi.org/10.1016/j.jechem.2020.02.033>.
- C. Li, Y. Huang, C. Chen, X. Feng, Z. Zhang, High-performance polymer electrolyte membrane modified with isocyanate-grafted Ti³⁺ doped TiO₂ nanowires for lithium batteries, *Appl. Surf. Sci.* 563 (2021) 150248, <https://doi.org/10.1016/j.apsusc.2021.150248>.
- E. Zhao, Y. Guo, A. Zhang, H. Wang, G. Xu, Polydopamine coated TiO₂ nanofiber fillers for polyethylene oxide hybrid electrolytes for efficient and durable all solid state lithium ion batteries, *Nanoscale* 14 (2022) 890–897, <https://doi.org/10.1039/D1NR06636F>.
- C. Liu, J. Wang, W. Kou, Z. Yang, P. Zhai, Y. Liu, W. Wu, J. Wang, A flexible, ion-conducting solid electrolyte with vertically bicontinuous transfer channels toward high performance all-solid-state lithium batteries, *Chem. Eng. J.* 404 (2021) 126517, <https://doi.org/10.1016/j.cej.2020.126517>.
- X. Yin, L. Wang, Y. Kim, N. Ding, J. Kong, D. Safanama, Y. Zheng, J. Xu, D.V. M. Repaka, K. Hippalgaonkar, S.W. Lee, S. Adams, G.W. Zheng, Thermal conductive 2D boron nitride for high-performance all-solid-state lithium-sulfur batteries, *Adv. Sci.* 7 (2020) 2001303, <https://doi.org/10.1002/adv.202001303>.
- K. Liu, H. Cheng; Z. Wang; Y. Zhao; Y. Lv; L. Shi; X. Cai; Z. Cheng; H. Zhang; S. Yuan, A 3 μm-ultrathin hybrid electrolyte membrane with integrative architecture for all-solid-state lithium metal batteries, *Adv. Energy Mater.* 2303940, doi: <https://doi.org/10.1002/aenm.202303940>.
- C. Li, Y. Huang, X. Feng, Z. Zhang, H. Gao, J. Huang, Silica-assisted cross-linked polymer electrolyte membrane with high electrochemical stability for lithium-ion batteries, *J. Colloid Interface Sci.* 594 (2021) 1–8, <https://doi.org/10.1016/j.jcis.2021.02.128>.
- L. Gao, N. Wu, N. Deng, Z. Li, J. Li, Y. Che, B. Cheng, W. Kang, R. Liu, Y. Li, Optimized CeO₂ nanowires with rich surface oxygen vacancies enable fast Li-ion conduction in composite polymer electrolytes, *Energy Environ. Mater.* 6 (2023) e12272, <https://doi.org/10.1002/eem2.12272>.
- F. Wu, Z. Wen, Z. Zhao, J. Bi, Y. Shang, Y. Liang, L. Li, N. Chen, Y. Li, R. Chen, Double-network composite solid electrolyte with stable interface for dendrite-free Li metal anode, *Energy Storage Mater.* 38 (2021) 447–453, <https://doi.org/10.1016/j.ensm.2021.03.020>.
- L. Liu, J. Lyu, J. Mo, H. Yan, L. Xu, P. Peng, J. Li, B. Jiang, L. Chu, M. Li, Comprehensively-upgraded polymer electrolytes by multifunctional aramid nanofibers for stable all-solid-state Li-ion batteries, *Nano Energy* 69 (2020) 104398, <https://doi.org/10.1016/j.nanoen.2019.104398>.
- L. Liu, J. Lyu, J. Mo, P. Peng, J. Li, B. Jiang, L. Chu, M. Li, Flexible, high-voltage, ion-conducting composite membranes with 3D aramid nanofiber frameworks for stable all-solid-state lithium metal batteries, *Sci. China Mater.* 63 (2020) 703–718, <https://doi.org/10.1007/s40843-019-1240-2>.
- S.-O. Tung, S. Ho, M. Yang, R. Zhang, N.A. Kotov, A dendrite-suppressing composite ion conductor from aramid nanofibres, *Nat. Commun.* 6 (2015) 6152, <https://doi.org/10.1038/ncomms7152>.
- M. Wang, C. Wang, Z. Fan, G. Wu, L. Liu, Y. Huang, Aramid nanofiber-based porous membrane for suppressing dendrite growth of metal-ion batteries with enhanced electrochemistry performance, *Chem. Eng. J.* 426 (2021) 131924, <https://doi.org/10.1016/j.cej.2021.131924>.
- M. Yang, K. Cao, L. Sui, Y. Qi, J. Zhu, A. Waas, E.M. Arruda, J. Kieffer, M. D. Thouless, N.A. Kotov, Dispersions of aramid nanofibers: a new nanoscale building block, *ACS Nano* 5 (2011) 6945–6954, <https://doi.org/10.1021/nn2014003>.
- X. Yang, K.R. Adair, X. Gao, X. Sun, Recent advances and perspectives on thin electrolytes for high-energy-density solid-state lithium batteries, *Energy Environ. Sci.* 14 (2021) 643–671, <https://doi.org/10.1039/D0EE02714F>.
- J. Wu, Z. Rao, Z. Cheng, L. Yuan, Z. Li, Y. Huang, Ultrathin, flexible polymer electrolyte for cost-effective fabrication of all-solid-state lithium metal batteries, *Adv. Energy Mater.* 9 (2019) 1902767, <https://doi.org/10.1002/aenm.201902767>.
- T. Wei, Z.-H. Zhang, Z.-M. Wang, Q. Zhang, Y.-S. Ye, J.-H. Lu, Z.U. Rahman, Z.-W. Zhang, Ultrathin solid composite electrolyte based on Li_{6.4}La₃Zr_{1.4}Ta_{0.6}O₁₂/PVDF-HFP/LiTFSI/Succinonitrile for high-performance solid-state lithium metal batteries, *ACS Appl. Energy Mater.* 3 (2020) 9428–9435, <https://doi.org/10.1021/acsaem.0c01872>.
- Y. Gao, Z. Sun, C. Cui, H. Wang, W. Cao, Z. Hou, D. Zhu, Y. Yang, T. Zhang, An ultrathin, flexible solid electrolyte with high ionic conductivity enhanced by a mutual promotion mechanism, *ACS Appl. Mater. Interfaces* 14 (2022) 45373–45381, <https://doi.org/10.1021/acsmi.2c12136>.
- M. Zhou, R. Liu, D. Jia, Y. Cui, Q. Liu, S. Liu, D. Wu, Ultrathin yet robust single lithium-ion conducting quasi-solid-state polymer-brush electrolytes enable ultralong-life and dendrite-free lithium-metal batteries, *Adv. Mater.* 33 (2021) 2100943, <https://doi.org/10.1002/adma.202100943>.
- Y. Ma, J. Wan, Y. Yang, Y. Ye, X. Xiao, D.T. Boyle, W. Burke, Z. Huang, H. Chen, Y. Cui, Z. Yu, S.T. Oyakhire, Y. Cui, Scalable, ultrathin, and high-temperature-resistant solid polymer electrolytes for energy-dense lithium metal batteries, *Adv. Energy Mater.* 12 (2022) 2103720, <https://doi.org/10.1002/aenm.202103720>.
- L. Liu, D. Zhang, T. Yang, W. Hu, X. Meng, J. Mo, W. Hou, Q. Fan, K. Liu, B. Jiang, L. Chu, M. Li, Flexible ion-conducting membranes with 3D continuous nanohybrid networks for high-performance solid-state metallic lithium batteries, *J. Energy Chem.* 75 (2022) 360–368, <https://doi.org/10.1016/j.jechem.2022.08.036>.
- J. Zhang, X. Zang, H. Wen, T. Dong, J. Chai, Y. Li, B. Chen, J. Zhao, S. Dong, J. Ma, L. Yue, Z. Liu, X. Guo, G. Cui, L. Chen, High-voltage and free-standing poly(propylene carbonate)/Li_{6.75}La₃Zr_{1.75}Ta_{0.25}O₁₂ composite solid electrolyte for wide temperature range and flexible solid lithium ion battery, *J. Mater. Chem. A* 5 (2017) 4940–4948, <https://doi.org/10.1039/C6TA10066J>.
- K. Karthik, R. Murugan, Lithium garnet based free-standing solid polymer composite membrane for rechargeable lithium battery, *J. Solid State Electrochem.* 22 (2018) 2989–2998, <https://doi.org/10.1007/s10008-018-4010-3>.
- X. Da, J. Chen, Y. Qin, J. Zhao, X. Jia, Y. Zhao, X. Deng, Y. Li, N. Gao, Y. Su, Q. Rong, X. Kong, J. Xiong, X. Hu, S. Ding, G. Gao, CO₂-assisted induced self-assembled aramid nanofiber aerogel composite solid polymer electrolyte for all-solid-state lithium-metal batteries, *Adv. Energy Mater.* 14 (2024) 2303527, <https://doi.org/10.1002/aenm.202303527>.
- L. Liu, L. Chu, B. Jiang, M. Li, Li_{1.4}Al_{0.4}Ti_{1.6}(PO₄)₃ nanoparticle-reinforced solid polymer electrolytes for all-solid-state lithium batteries, *Solid State Ion.* 331 (2019) 89–95, <https://doi.org/10.1016/j.ssi.2019.01.007>.
- X. Meng, D. Zhang, J. Mo, L. Liu, T. Yang, Q. Fan, Q. Zhao, R. Zhou, M. Zhang, W. Hou, W. Hu, W. Zhang, Y. Jin, B. Jiang, L. Chu, M. Li, Room-temperature solid-state metallic lithium batteries based on high-content boron nitride nanosheet-modified polymer electrolytes, *Appl. Surf. Sci.* 648 (2024) 158962, <https://doi.org/10.1016/j.apsusc.2023.158962>.
- Z. Li, S. Wang, J. Shi, Y. Liu, S. Zheng, H. Zou, Y. Chen, W. Kuang, K. Ding, L. Chen, Y.-q. Lan, Y.-p. Cai, Q. Zheng, A 3D interconnected metal-organic framework-derived solid-state electrolyte for dendrite-free lithium metal battery, *Energy Storage Mater.* 47 (2022) 262–270, <https://doi.org/10.1016/j.ensm.2022.02.014>.
- J. Cheng, G. Hou, Q. Chen, D. Li, K. Li, Q. Yuan, J. Wang, L. Ci, Sheet-like garnet structure design for upgrading PEO-based electrolyte, *Chem. Eng. J.* 429 (2022) 132343, <https://doi.org/10.1016/j.cej.2021.132343>.
- E. Zhao, Y. Guo, Y. Liu, S. Liu, G. Xu, Nanostructured zeolitic imidazolate framework-67 reinforced poly(ethylene oxide) composite electrolytes for all solid state Lithium ion batteries, *Appl. Surf. Sci.* 573 (2022) 151489, <https://doi.org/10.1016/j.apsusc.2021.151489>.
- L. Chen, X. Qiu, Z. Bai, L.-Z. Fan, Enhancing interfacial stability in solid-state lithium batteries with polymer/garnet solid electrolyte and composite cathode

- framework, *J. Energy Chem.* 52 (2021) 210–217, <https://doi.org/10.1016/j.jechem.2020.03.052>.
- [44] Y. Li, Y. Qin, J. Zhao, M. Ma, M. Zhang, P. Li, S. Lu, H. Bu, K. Xi, Y. Su, S. Ding, Boosting the ion mobility in solid polymer electrolytes using hollow polymer nanospheres as an additive, *ACS Appl. Mater. Interfaces* 14 (2022) 18360–18372, <https://doi.org/10.1021/acsami.2c00244>.
- [45] Q. Guo, F. Xu, L. Shen, Z. Wang, J. Wang, H. He, X. Yao, Poly(ethylene glycol) brush on $\text{Li}_{6.4}\text{La}_3\text{Zr}_{1.4}\text{Ta}_{0.6}\text{O}_{12}$ towards intimate interfacial compatibility in composite polymer electrolyte for flexible all-solid-state lithium metal batteries, *J. Power Sources* 498 (2021) 229934, <https://doi.org/10.1016/j.jpowsour.2021.229934>.
- [46] L. Han, J. Wang, X. Mu, T. Wu, C. Liao, N. Wu, W. Xing, L. Song, Y. Kan, Y. Hu, Controllable magnetic field aligned sepiolite nanowires for high ionic conductivity and high safety PEO solid polymer electrolytes, *J. Colloid Interface Sci.* 585 (2021) 596–604, <https://doi.org/10.1016/j.jcis.2020.10.039>.
- [47] C. Li, Y. Huang, C. Chen, X. Feng, Z. Zhang, P. Liu, A high-performance solid electrolyte assisted with hybrid biomaterials for lithium metal batteries, *J. Colloid Interface Sci.* 608 (2022) 313–321, <https://doi.org/10.1016/j.jcis.2021.09.113>.
- [48] M. Arrese-Igor, M. Martínez-Ibañez, E. Pavlenko, M. Forsyth, H. Zhu, M. Armand, F. Aguesse, P. López-Aranguren, Toward high-voltage solid-state li-metal batteries with double-layer polymer electrolytes, *ACS Energy Lett.* 7 (2022) 1473–1480, <https://doi.org/10.1021/acseenergylett.2c00488>.
- [49] Z. Yao, K. Zhu, X. Li, J. Zhang, J. Chen, J. Wang, K. Yan, J. Liu, 3D poly(vinylidene fluoride–hexafluoropropylene) nanofiber-reinforced PEO-based composite polymer electrolyte for high-voltage lithium metal batteries, *Electrochim. Acta* 404 (2022) 139769, <https://doi.org/10.1016/j.electacta.2021.139769>.
- [50] L. Wang, H. Shi, Y. Xie, Z.-S. Wu, Fluorinated boron nitride nanosheet enhanced ultrathin and conductive polymer electrolyte for high-rate solid-state lithium metal batteries, *Interdiscip. Mater.* 2 (2023) 789–799, <https://doi.org/10.1002/idm2.12121>.
- [51] A. Chen, Q. Zeng, W. Wen, X. Wen, Z. Li, Y. Liu, J. Guan, H. Wang, W. Liu, P. Chen, L. Zhang, A highly salt-soluble ketone-based all-solid-state polymer electrolyte with superior performances for lithium-ion batteries, *ACS Appl. Mater. Interfaces* 15 (2023) 17791–17800, <https://doi.org/10.1021/acsami.2c22228>.